Radiation Mediated Shock and Planar Shock Breakout in the Presence of Atomic Transition Lines

Jonathan Morag[1]

[1] *Weizmann Institute of Science*
234 Herzl St.
Rehovot, Israel

ABSTRACT

We numerically study fast Newtonian radiation mediated shocks (RMS - $v/c \lesssim 0.2$) in two simplified problems within the context of supernova shock breakout; (1) An RMS traveling in a uniform medium, and (2) an RMS escaping a powerlaw density profile in planar geometry ($\rho \propto x^n$). Both problems were previously solved in the literature assuming a fully ionized plasma medium, emitting and absorbing photons primarily via Bremstrahlung. It was shown that at high shock velocities, Bremstrahlung photon production in the fully ionized scenario is insufficient for achieving local thermal equilibrium (LTE) at the shock front, and as a result the photons can reach Compton equilibrium with electrons temperatures of many keV.

In this study we incorporate, for the first time, opacity from bound species of heavy elements (solar-like composition) into these two problems, at times drastically augmenting the photon production due to the addition of bound-free and bound-bound radiative processes. We solve the problem using a previously developed hydrodynamically coupled multi-group radiative diffusion code, including inelastic Compton scattering and frequency-dependent opacity from the publicly available TOPS table.

We show that the addition of a more realistic opacity leads the radiation to maintain LTE at higher velocities in comparison to the fully ionized problem. In the planar SBO problem this can lead to typically a factor of 2 lower temperature and at times orders of magnitude. This result is important for the observation of supernova shock breakout emission, where strong deviations from LTE and strong X-ray emission were previously predicted for a significant fraction of the parameter space for simple envelope breakout. The SED of SN envelope breakout will very likely remain in LTE for explosions in red super giant stars without stellar wind (and part of blue super giant star explosions), making X-Ray observations less likely in these cases by orders of magnitude relative to previous predictions. We provide a simple semi-analytic description for the SED in the case where LTE is maintained.

A correct calculation of shock-breakout radiation requires opacity tables that include bound yet highly ionized species, ruling out the use of certain line tables (such as the commonly used Kurucz table) for use in the shock breakout problem.

Keywords: radiation: dynamics– shock waves– supernovae: general

1. INTRODUCTION

In core-collapse supernovae (SNe), an explosion in the interior of massive stars launches a radiation mediated shock (RMS) that traverses outwards through the stellar envelope. When the shock reaches the outer edge of the progenitor star or the surrounding material to within an optical depth of $\tau \sim c/v$, a luminous 'shock break-

out' (SBO) pulse is emitted. In the case of a spherical 'envelope breakout' (without surrounding wind or 'circumstellar' material) the pulse is predicted to last tens of minutes to an hour, with a luminosity of $\sim 10^{45}$ erg s^{-1}, peaking in the UV/X-Ray (see Waxman & Katz 2016; Levinson & Nakar 2020, for a review). Due to the short time span of the breakout pulse, only a few such SBO candidates have been observed to date (Campana et al. 2006; Soderberg et al. 2008; Gezari et al. 2010, 2015).

Multiple wavelength breakout observations can shed light on the properties of the progenitor star and its

jmorag88@gmail.com

surrounding environment immediately prior to the explosion. In particular, the extent of wind and circumstellar material present for each SN type is partially undetermined, despite indication of wind interaction in observed lines and X-ray following SBO (Smith 2014; Bruch et al. 2021; Dwarkadas 2014; Huang et al. 2018; Margutti et al. 2013), and direct observation of a few optically thick ($\tau \gtrsim c/v$) 'wind-breakout' events (Ofek et al. 2014; Zimmerman et al. 2023)[1]. Upcoming telescope projects should together provide multiwavelength observations of 10's of SBO's in the coming years allowing systematic study, including the Vera Rubin observatory in the optical (Ivezić et al. 2019), the ULTRASAT UV space mission (Shvartzvald et al. 2023), and the recently launched Einstein probe X-ray mission (Yuan et al. 2022). UV and X-ray observations are particularly important for determining SBO temperatures. This data should be interpreted with a self-consistent frequency-dependent model of SBO emission, which is currently not available.

The observed spectrum at SBO is determined by the properties of the radiation mediated shock as it reaches the edge of the stellar material. At high temperatures, the medium is nearly fully ionized, and the dominant photon production mechanism is Bremsstrahlung. Bremstrahlung emission can be insufficient for producing photons at high shock velocities, leading to deviations from local thermal equilibrium (LTE) and high temperatures of many keV. The temperature of RMS and SBO in this case of fully-ionized medium emitting Bermsstrahlung has been solved in the literature (Blandford & Payne 1981; Weaver 1976; Katz et al. 2010; Sapir et al. 2013; Sapir & Halbertal 2014). Other works study SBO in a partially ionized medium with additional emission/absorption processes, but do not include inelastic Compton scattering. These include works employing the multigroup STELLA radiative transfer code (Blinnikov et al. 2000; Tominaga et al. 2011; Förster et al. 2018; Kozyreva et al. 2020), which incorporates atomic transition lines based on the Kurucz line list (Kurucz 1995). The omission of inelastic Compton scattering is reasonable in certain parts of the parameter space (e.g. Kozyreva et al. 2020, as discussed

in Morag et al. 2024), but inappropriate for others, as we discuss below. See also Sapir & Halbertal (2014) for further comparison of varied SBO temperature results in the literature.

In this work we numerically study the nonrelativistic uniform RMS and planar SBO problems, useful analogs for the envelope SBO problem. In the planar SBO, we study two separate initial density profiles, representative of the profiles in red super giant and blue supergiants stars (RSG,BSG), the likely progenitors of type II and 1987a-like SNe. We include for the first time together in these problems, both inelastic Compton scattering (Kompaneets equation), and frequency-dependent emission and absorption due to radiative photo-ionization ('bound-free') and atomic transition lines ('bound-bound'). We employ a previously developed one-dimensional radiative diffusion code, coupled with hydrodynamics (Sapir & Halbertal 2014; Morag et al. 2024, hereafter SH14,M24). Radiative processes are handled with a 'multi-group' treatment, where the photon flux and energy distribution is binned into frequency groups, and the physics of each group is solved separately. Our code employs the publicly available TOPS opacity table by Los Alamos National Labs (LANL). We verify our results in the case where line opacity is unimportant against results in the literature (Katz et al. 2010; Sapir et al. 2013; Sapir & Halbertal 2014), finding good agreement.

Our results consolidate existing approaches in the literature described above, showing that SBO at lower temperatures and velocities will be affected by the presence of lines and remain near local thermal equilibrium. Then, for faster shocks, behavior will transition towards bulk Comptonization. We will show that for the transition region and at temperatures and velocities below it, the observed temperature is at least a factor of two lower than the predictions of Bulk Comptonization. This reduction of temperature has important consequences regarding the prediction for X-ray flashes in envelope breakout (less so for GRB's), and may eventually provide an additional test for the extent of circumstellar material in RSG's.

We do not address relativistic effects that become important at high velocities and temperatures, such as pair production (Budnik et al. 2010; Nakar & Sari 2012; Ito et al. 2020a,b). We also do not examine the windbreakout case, where the possible presence of collisionless shocks can yield a strong deviation from LTE behavior and many keV temperatures (Waxman & Loeb 2001; Katz et al. 2011; Murase et al. 2014; Wasserman et al. 2025).

---

[1] A recent systematic study of optical emission in type II SNe from red super giants suggested that roughly two-thirds of objects do not exhibit wind interaction during the hours and days following SBO (Irani et al. 2023). Type Ic/Ibc SNe where the prognitor has likely undergone significant mass loss are associated with X-ray flashes (XRF) and low-luminosity gamma-ray bursts (ll-GRB), indicative of relativistic breakout and/or circumstellar interaction (Campana et al. 2006; Soderberg et al. 2008; Starling et al. 2011).

This paper is structured as follows. In § 2 we describe our numerical code, including details of the frequency-dependent opacity. In § 3.1 we study the uniform RMS problem, including describing initial conditions in § 3.2 and the temperature results in § 3.3. In § 4 we perform a similar analysis for the planar shock breakout, with temperature results in § 4.3. In § 5 we address the finite frequency resolution in our code relative to the line resolution. In § 6 we discuss the impact of our theoretical results on upcoming observations, particularly in the X-ray bands. We discuss and summarize in § 7.

2. NUMERICAL DETAILS - HYDRODYNAMICS EQUATIONS

In both the uniform RMS and the planar SBO problems we use a numerical code previously described in M24 and in SH14. Our code describes the evolution of Lagrangian matter density ρ, velocity v, matter pressure p, and radiation energy and flux u_ν and j_ν. u_ν and j_ν are calculated using a 'multigroup' treatment, where the photons are binned into energy groups and the radiation physics is solved separately for each group. In all simulations we include compression of the radiation and plasma, radiative diffusion, radiative emission and absorption, as well as inelastic Compton scattering via the Kompaneetz equation.

The governing equations of our code describing the evolution with the above processes are given by equations 24-36 in M24. We make two small substitutions in these equations to account for the planar geometry (as opposed to spherical geometry in M24). First, we substitute $\nabla \cdot f = \frac{1}{r^2} \frac{\partial (r^2 f)}{\partial r} \to \frac{\partial f}{\partial r}$ in their equations 30-32, 36, where f is an arbitrary function. Second, we change their equation 25 to

$$\rho = \rho_{\text{init}} \frac{\partial r_{\text{init}}}{\partial r}, \tag{1}$$

where ρ_{init} and r_{init} are the initial position and density (denoted with a subscript 0 in M24). The rest of the equations are used in our code as written.

We produce two types of simulations with our code, each employing a different choice of frequency-dependent opacity. In one type (henceforth denoted 'free-free only'), we choose that the emission and absorption opacity $\kappa_{\text{abs},\nu}$ only includes Bremsstrahlung (given analytically in SH14 equations 7-9). In the other set of simulations we use a coarse multi-group frequency average of $\kappa_{\text{abs},\nu}$, the high-frequency resolution TOPS opacity table. As is done in M24, we differentiate in our governing equations between the frequency-dependent diffusion opacity κ_*, employed in M24 equations 26 and 33, and the frequency dependent emission / absorp-

tion opacity κ_{abs} used in their equation 29. The diffusion opacity is given by, $\kappa_*^{-1} = (\Delta\nu_{\text{bin}})^{-1} \int d\nu (\kappa_{\text{es}} + \kappa_{\text{abs},\nu})^{-1}$, where κ_{es} is the Thomson scattering opacity and $\Delta\nu_{\text{bin}}$ is the width of the binned frequency group in the simulation. Meanwhile, the absorption opacity of each group is given by $\kappa_{\text{abs}} = (\Delta\nu_{\text{bin}})^{-1} \int d\nu \kappa_{\text{abs},\nu}$. In the free-free only simulations, analytic values sampled at each group are used both in κ_* and in κ_{abs}, without performing an average.

The numerical scheme and the time-step limitations are the same as in M24 sec. 3.2. In TOPS simulations we include the 'protections' on diffusive and radiative transfer, including the addition of a flux limiter, previously described in M24 sec. 3.2.2 (their equations 40-41).

We assume everywhere a solar composition of elements, and use a slightly simpler equation of state for the matter energy and pressure, which does not include latent energy of ionization, without affecting our conclusions. Namely, the matter energy density, temperature and pressure are related by

$$e = \left(\frac{1}{\gamma - 1}\right) p, \ p = (\rho/\mu)T, \ \mu = m_{\text{amu}} / \sum_i (1 + Z_i) x_i / A_i \tag{2}$$

where γ is adiabatic index, approximated as 5/3, m_{amu} is the atomic mass unit, x_i, and A_i are the mass fraction and atomic mass of element i, Z_i is the atomic number.

For later use we define the equivalent LTE temperature T_{LTE} as

$$T_{\text{LTE}} = (u/a_{\text{BB}})^{1/4}, \tag{3}$$

where u is the frequency integrated photon energy density, and a_{BB} is the Boltzmann blackbody constant. We also introduce an approximate photon temperature defined by the photon energy distribution u_ν (Zel'dovich & Raizer 2002).

$$T_\gamma = \frac{1}{4u} \int_0^\infty \left[h\nu u_\nu + \frac{c^3}{8\pi} \left(\frac{u_\nu}{\nu}\right)^2 \right] d\nu \tag{4}$$

The latter two temperatures are equivalent when the radiation is in LTE, and T_γ matches the plasma temperature T_{e} when the two are either in LTE or in Compton equilibrium.

2.1. The Opacity Table

The TOPS opacity table (Colgan et al. 2018) is to our knowledge the only publicly available source for frequency-dependent opacity that includes highly ionized species. The table is experimentally verified, though at densities much higher ($\sim 10^{-2} - 10^{-3}$ g cm^{-3} Colgan et al. 2015, 2016, 2018) than we solve for in our problem ($10^{-11} - 10^{-7}$ g cm^{-3}). Thus, the existence of

individual lines or atomic states used in TOPS is not assured, though we are concerned here with the ensemble behavior describing the general SED, and delayed deviations from LTE due to the cumulative presence of atomic lines. The table assumes thermal equilibrium between the plasma and the radiation, and does not include 'expansion opacity effects' (see § 7).

Unlike our previous use of the table in Morag et al. (2023, 2024), our downloaded TOPS Opacity table contains all elements up to and including Zn (with the exception of Li, Be, and B). Adding heavy elements, despite their very low abundance, turned out to be important at high (10's-100's eV) temperatures due to the admittance of highly ionized (but not fully ionized) states and their associated lines. We also note that the TOPS table we downloaded is capped at $h\nu = 10^4$ eV. In cases where higher frequencies were needed, we complemented the table with analytic Bremstrahllung-only opacity at $h\nu > 10^4$ eV. TOPS is limited in resolution with regards to the underlying temperature, density, and frequency grid. This limitation can lead to crashes in numerics and impacts our ability to test convergence, especially since the frequency resolution is at least an order of magnitude coarser than the width of individual lines (see § 7).

3. UNIFORM RADIATION MEDIATED SHOCK

3.1. *U-RMS Introduction*

In the steady-state non-relativistic uniform radiation mediated shock (RMS) problem, a strong shock traverses a uniform plasma medium at velocity $\beta_0 = v_0/c$ in planar geometry. The medium is assumed to be highly ionized or fully ionized. Energy and momentum are dominated by photons undergoing diffusion with scattering opacity $\kappa_{es} \sim \sigma_T/m_i$, where σ_T is the Thomson cross section, and m_i is the mass of the dominant ion in the plasma (e.g. the proton mass for Hydrogen).

Hydrodynamics for the fully-ionized RMS was solved by Weaver (1976). In the shock frame, cold 'upstream' plasma heading towards the shock at velocity v_0, collides with hot plasma at slower velocity, $v_0 \left(\frac{\gamma-1}{\gamma+1}\right) = v_0/7$, and gets swept 'downstream'. The upstream protons and ions transfer their energy and momentum to the photons across a length scale $l \sim (\rho\kappa_{es}\beta_0)^{-1}$, which determines the thickness of the shock. This scale, across which the plasma decelerates, also coincides with the distance to which photons diffuse upstream against the flow. Correspondingly, the scattering optical depth across the shock is $\tau \sim l(\rho\kappa)^{-1} \sim c/v$ and the shock-crossing time-scale is $t_0 \sim c/\rho\kappa v_0^2$ (Katz et al. 2010).

As the plasma heats up across the shock, it emits (and absorbs) photons. The hydrodynamics and total energy density are insensitive to the exact photon production

mechanism, but the radiative energy density distribution u_ν and the plasma temperature[2] T can be greatly effected. If emission (and absorption) processes are efficient relative to the shock crossing timescale, the radiation will maintain a Planck distribution $B_\nu(T)$ throughout. In such a scenario, the local temperature will everywhere be given by

$$T_{\text{LTE,W}} = [3P_W/a_{BB}]^{1/4} \qquad (5)$$

where $a_{BB} = 8\pi^5/15(hc)^3$ and $P_W(r,t)$ is the pressure, as described by the Weaver steady-state analytic solution (Weaver 1976; Katz et al. 2010; Sapir & Halbertal 2014).

For Bremsstahlung emission, the opacity is highest at lowest frequencies, and behaves like $\kappa_\nu \propto \nu^{-2}$. At faster velocities where the emission (and absorption) are inefficient, there exists a critical frequency $h\nu_c$ (Katz et al. 2010, hereafter KBW10), above which emitted photons will undergo significant inelastic Compton scattering with the hot electrons before being reabsorbed again[3]. Photons below $h\nu_c$ will thermalize with the electrons, forming the Rayleigh Jeans tail of a Planck distribution $B_\nu(T)$. Photons above $h\nu_c$ will up-scatter to $\sim 3T$ energies, forming a Wien peak. T in turn -assuming Comptonized photons dominate the energy density- is determined by the equation of state $T = p_\gamma/n_\gamma$, where p_γ, n_γ are the photon pressure and number density of Comptonized photons. Since $p_\gamma = p_W$ depends only the hydrodynamics and is insensitive to photon production, the temperature in the up-scattered Wien peak is determined inversely by the photon production rate Q_{eff}. The Q_{eff} is integrated in frequency from all photons emitted at $h\nu > h\nu_c$ and for the case of Bremsstrahlung opacity only, is given by (KBW10)

$$Q_{\text{eff}} \approx \alpha_e n_i n_e \sigma_T c \sqrt{\frac{m_e c^2}{T}} \Lambda_{\text{eff}} g_{\text{eff}}, \qquad (6)$$

where n_i and n_e are the number densities of ions and free electrons, and σ_T is the Thomson cross-section, m_e is the electron mass and c is the speed of light. The coefficient $\Lambda_{\text{eff}} \sim \log(\lambda)$ and the effective gaunt factor $g_{\text{eff}}(\lambda)$, both result from integrating the emission from $h\nu_c$ to $+\infty$ and are a weak function of $\lambda = T/h\nu_c$. We note that the description of Q_{eff} for $\dot{n}_\gamma$ is approximate since it assumes that all the photons are Wien distributed and

---

[2] The plasma temperature T, represents the temperature of both the electrons and the ions, which are assumed to be in thermal equilibrium throughout, a reasonable assumption in this scenario.

[3] Efficient Compton scattering requires that the y parameter at the shock, $y = (4T/m_e c^2)\tau_{es}^2 > 1$, which generally holds for the relevant part of the parameter space.

that photon absorption for $h\nu > h\nu_c$ is negligible. We show below that these approximations are reasonable for a large part of our parameter space.

KBW10 provide analytic descriptions for the deviations in temperature from LTE in steady state. From peak Compton temperature T_{peak} near the shock, photon production will reduce the temperature towards T_{LTE} in the far downstream across a thermalization length scale $L_T \sim v_0 n_{\gamma,peak}/Q_\gamma$ (assuming uniform photon production rate $Q_{eff}(\tau > 0) = Q_{eff}(T_{peak})$, where $\tau > 0$ represents the downstream optical depth). Therefore, by comparing L_T to the shock width l, we arrive at a velocity cutoff $\beta_{0,cut}$ above which T will deviate from T_{LTE} to higher temperatures (KBW10). Namely,

$$\beta_{0,cut} > 0.7 n_{p,15}^{1/30} (\Lambda_{eff} g_{eff})^{4/15}, \qquad (7)$$

where $n_p = n_{p,15} 10^{15} \mathrm{g\,cm^{-3}}$ is the proton density. Likewise, we may estimate a relationship between the peak temperature and the shock velocity, given by

$$\beta_{0,K10} \approx 0.2 \left(\Lambda_{eff} g_{eff}/2\right)^{1/4} \left(T_{peak}/10\,\mathrm{keV}\right), \qquad (8)$$

where $\Lambda_{eff}(\lambda)$ and $g_{eff}(\lambda)$ can be solved for self-consistently. These results agree with Weaver (1976) for $T < 50 keV$.

KBW10 also provide an ODE description that solves for the number density of photons $n_\gamma(\tau)$ in steady-state under similar assumptions to the heuristic analytic solutions, and arrive at similar results. Here we rewrote these relations for the case of a general plasma composition, in lieu of a Hydrogen only composition as was done in KBW10. We note that for the Hydrogen-dominated (but not Hydrogen-only) envelope that we tested here, the result for the Bremsstrahlung only case is nearly unaffected by the presence of other elements.

3.2. *Initial and Boundary conditions*

The calculation describes a constant velocity piston being driven into a cold medium of uniform density ρ_0, driving a radiation mediated shock with velocity $v_0 = \beta_0 c$[4]. For faster convergence, the simulation is started with the analytic RMS solution (Weaver 1976; Sapir & Halbertal 2014, Appendix C). After several shock crossings, whose number depends on the opacity and on the velocity, the shock reaches steady state, both in hydrodynamics and in temperature. Higher shock velocities in the free-free only case require many shock crossings, up to ~ 150 in order to reach steady state. The system is built large enough so that the

shock will not reach the edge prior to arriving in steady state. The initial plasma temperature is $T_{LTE,W}$ (equation 5), and the corresponding radiation distribution is given $u_\nu = 4\pi B_\nu(T_{LTE,W})/c$, where B_ν is the Planck intensity.

We use a constant initial spatial grid. Simulations vary in grid spacing between 15 and 60 spatial grid points per shock crossing and a multigroup frequency grid of $\Delta\nu/\nu \sim 0.07 - 0.25$. At steady state, all sims are converged to better than a percent in ρ, v, p, as well 3% in peak T and $10's$ of percent in u_ν at individual frequencies.

Convergence of the temperature peak in the ff-only case, requires very low initial temperatures in the upstream due to the strong dependence of photon count on temperature (for numerical reasons the upstream temperature cannot be set identical to zero). When using TOPS instead, the highest possible temperature for the cold matter is taken, $T_{init} > 1eV$, while ensuring that $u_{ph,upstream} \ll u_{ph,downstream}$ and that the results are not effected. Inelastic Compton scattering and bound-free and bound-bound opacity (where relevant) are turned on gradually, over roughly a shock crossing time to avoid numerical issues.

3.3. *U-RMS Temperature Results*

In this section we present numeric results showing the effect of opacity on the uniform RMS problem. For each choice of parameters, we produce two sets of simulations, with and without the effect of bound-free and bound-bound processes in the opacity. This change affects the plasma temperature T and photon energy distribution u_ν, but has negligible effect on the radiation pressure $p_\gamma \propto \int u_\nu d\nu$, which dominates the total pressure p. Converged simulation results agree in (ρ, v, p) with the analytic Weaver solution (Weaver 1976; Sapir & Halbertal 2014, Appendix C) to 2% or better[5]. In the inset to figure 1, we show an example of a steady-state velocity profile in a simulation compared with the analytic RMS solution (Weaver 1976; Sapir & Halbertal 2014).

Figures 1 and 2 show an example with parameters ($\beta_0 = 0.1$, $\rho_0 = 10^{-9}\,\mathrm{g\,cm^{-3}}$). We first examine the result in presence of free-free opacity only. Figure 1 provides a snapshot of the steady-state temperature across the shock. In the case where only free-free opacity is present (dashed lines), plasma and photons temperatures T and T_γ at the shock and downstream of it are nearly matched in Compton equilibrium. The tempera-

---

[4] Corresponding piston velocity in the unshocked plasma frame is $(6/7)v_0$

[5] In the cases $\beta = 0.2 - 0.25$, $\rho_0 = 10^{-7}\,\mathrm{g\,cm^{-3}}$ with free-free opacity only, pressure agrees with the analytic solution to 3%.

ture deviates largely from T_{LTE}, reaching peak temperatures near the shock of ~ 800 eV before settling into equillibrium ($T_{\mathrm{LTE}} \sim 160$ eV) in the far downstream. Our free-free only results are in close agreement with the results of SH14, figure 1 ($\beta = 0.1$, number of protons $n_p = \rho_0/m_{\mathrm{p}} = 10^{17}\,cm^{-3}$). In SH14 they solve a hydrogen only problem, and get similar results, since Bremstrahllung opacity is insensitive to metallicity. We also observe a low energy density radiative precursor (in agreement with SH14 - see their discussion).

Figure 2 shows cross sections of the radiation energy density distribution u_ν, in the vicinity of the shock. In the case of free-free opacity only (again in dashed lines), u_ν at the shock approaches Compton equilibrium with a corresponding Wien peak (red dashed line). Near downstream of the shock (yellow dashed line), u_ν approaches LTE. Meanwhile, in the near upstream, diffusion of photons from the shock leads u_ν to exhibit a similar (though less prominent) high-frequency peak (blue dashed line). The latter is the high temperature, but relatively low energy radiative precursor.

Returning to figure 1, we compare the temperature result for $\beta = 0.1$ (free-free only) to the semi-analytic ODE estimate presented in KBW10 (dashed teal line), which assumes Compton equilibrium with an equation of state $P = n_\gamma T$, where n_γ is the number density of photons. We find good agreement between the ODE and the sims at the shock and immediately downstream of it, where the radiation in the simulation is near Compton equilibrium. Peak temperature in the ODE is in general up to 30% lower than the temperature observed in the simulation, primarily since a non-negligible a fraction of the energy and photons lie outside of the Wien peak at lower frequencies (e.g. red dashed line in figure 2). Q_{eff} in the ODE also agrees with $\dot{n}$ from the simulation to 10's % or better. The far downstream temperature in the ODE progresses towards T_{LTE}, due to a heuristic suppression factor on the photon production, leading the net photon production to be zero when $T_{\mathrm{ODE}} = T_{\mathrm{LTE}}$. The details of our implementation of the ODE are presented in the appendix.

In figure 2 again, we compare the result at $\tau = 0$ to a Wien spectrum using (T, u) derived from the semi-analytic ODE estimate (teal dashed line - KBW10). We find very good agreement at the Wien peak. We compare the low-frequency end at the location with a Planck energy density $B_\nu(T)$, using the same T from the ODE. We again find excellent agreement, since the low frequency photons are in thermal equilibrium with the plasma due to the large Bremstrahllung opacity κ_ν.

When we introduce the bound-free and bound-bound opacity using TOPS (solid lines in figures 1 and 2) the
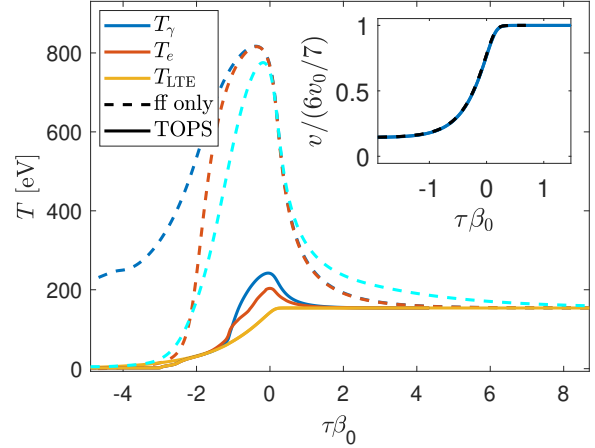

Figure 1. Temperature profile of a steady-state RMS as a function of optical depth, for a shock velocity $\beta_0 = 0.1$ and initial density $\rho_0 = 10^{-9}\,\mathrm{g\,cm^{-3}}$. Photon temperature T_γ (equation 4 - in blue) and plasma temperature T (in red) are markedly lower in the presence of TOPS opacity (solid lines) relative to the ff-only case (dashed lines). T_{LTE} (equation 3 in yellow) is nearly identical for both cases. ff-only simulation results agree with the result of an ODE integration, described in the appendix of KBW10 (dashed teal lines). The dashed ff-only results agree with figure 1 in SH14. Inset shows simulation velocity in the shock frame for both the ff-only and TOPS case (both in blue), against the analytic Weaver solution (black dashed), all collapsed on top of each other. $\tau = 0$ is set to the point of maximum convergence of the flow and positive τ indicates downstream. $\tau\beta_0 = 1$ corresponds to one shock crossing width.

temperature is drastically different. Increased photon production reduces the temperature everywhere towards T_{LTE}, with minor deviations from LTE located at the peak (similar location to the previous peak). When the temperature does deviate from LTE, T and T_γ are not matched as in the free-free only case, since the spectrum is not dominated by a single Wien peak. The high-temperature radiative precursor disappears, as photons diffusing upstream are reprocessed.

In figure 3, we map peak electron temperature as a function of density and shock velocity for the cases of free-free only opacity and full opacity (blue dots and connecting line and yellow dots and connecting line). At the lowest shock velocities, temperature for both opacity choices remains remains close to (magenta line)

$$T_{\mathrm{LTE,p}} = \left(6\left(3\rho_0 v_0^2\right)/7a_{\mathrm{BB}}\right)^{1/4}. \tag{9}$$

As shock velocities increase past $\beta \sim 0.03$ in the free-free only case, peak temperature gradually increases away from T_{LTE} and follows equation 8 (green line) to 10's of percent. Equation 8 itself is in close (few percent) agree-
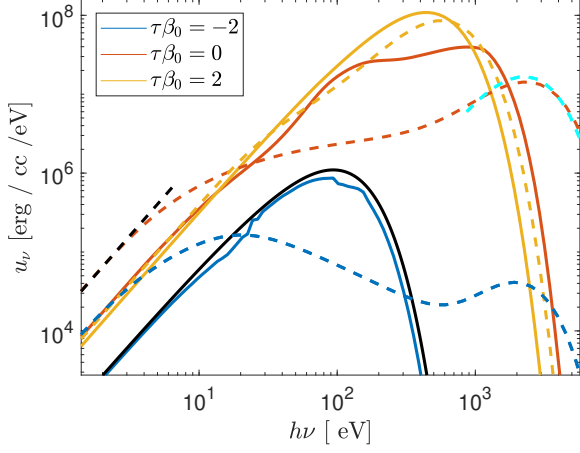
Figure 2. Steady-state photon energy density distribution, u_ν for the same simulations as in figure 1, showing that adding TOPS opacity reduces T_γ and brings the distribution closer to LTE. In the presence of ff-only opacity (dashed lines) u_ν reaches very high temperatures, matching Compton equillibrium (teal dashed line) based on T_γ from figure 1. u_ν cross-sections are shown at (-2,0,2) shock crossings from the point of max compression (with positive τ indicating downstream).

Figure 3. Mapping of peak electron temperature of as function of β_0, for three different densities. From top to bottom, the initial densities presented are $\rho_0 = 10^{-7}, 10^{-9}, 10^{-11}\,\mathrm{g\,cm^{-3}}$. For high velocities, calculations with free-free only opacity increase, in agreement with equation 8. The presence of TOPS opacity can significantly delay deviation from T_{LTE}, especially at lower densities. Every dot in the figure represents a converged calculation

ment with individual calculations of the ODE presented in KBW10 (green dots), based on similar assumptions.

The introduction of the TOPS opacity in figure 3 (yellow line) delays deviations from T_{LTE} in many parts of the parameter space. The relative effect of TOPS is mostly determined by temperature, to which the opacity is most sensitive. At highest densities ($\rho_0 = 10^{-7}\,\mathrm{g\,cm^{-3}}$), and therefore highest correspong temperatures $T_{\mathrm{LTE}} \propto (\rho_0 \beta_0^2 c^2)^{1/4}$, all elements are nearly fully ionized, and the TOPS opacity is similar to a Bremstrahllung-only opacity (example in figure 4 - red lines). Consequently, the deviation from the free-free only opacity in this case is minor. Meanwhile, at lower densities, the breakout temperature is lower, and the opacity is markedly different with TOPS (figure 4 - blue lines). In the case of $\rho_0 = 10^{-11}\,\mathrm{g\,cm^{-3}}$, simulations with TOPS remain in LTE for the entire parameter space that we checked, deviating by orders of magnitude from the temperature prediction in the presence of free-free only opacity. Figure 4 also includes Morag (2023) opacity tables for comparison (see discussion).

4. SHOCK BREAKOUT IN PLANAR GEOMETRY

4.1. *Planar SBO Introduction*

The problem of a shockwave escaping a power-law initial density profile $\rho_{\mathrm{init}} \sim x^n$, also known as the 'planar shock breakout problem', was introduced and solved by Sakurai (1960) and then later by
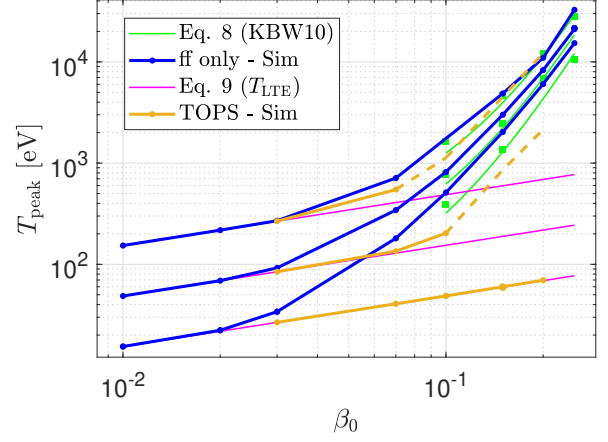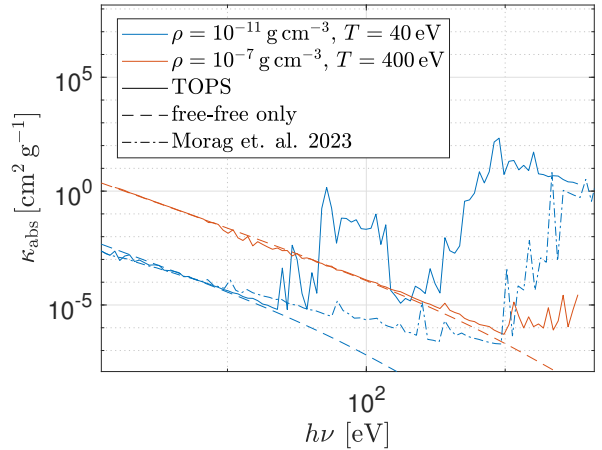

Figure 4. Example multigroup emission / absorption opacities at $T = (40, 400)$ eV, which correspond to T_{LTE} at velocity $\beta_0 = 0.07$ and densities $\rho = (10^{-7}, 10^{-11})\,\mathrm{g\,cm^{-3}}$ (see figure 3). The effect of TOPS opacity on photon production relative to free-free only opacity is pronounced at lower breakout temperatures, $T = 40$ eV, but has only a minor effect at $T = 400$ eV. The table from Morag (2023) is also shown at 40 eV, demonstrating a drastically different result due to use of the Kurucz table. Photon production drops roughly exponentially above the Planck peak frequency, located here at $h\nu \sim (100, 1000)$ eV.

Gandel'Man & Frank-Kamenetskii (1956). The shock structure and emitted luminosity for the case of a diffusive shock was solved by Sapir et al. (2011), by combining in an Anzats the Sakurai solution with the analytic Weaver RMS. The emitted temperature was calculated by Sapir et al. (2013) and the multi-group output spectrum in SH14, both assuming free-free emission.

As the shock travels towards the stellar edge ($x \to 0$), its velocity is given by

$$v_{\rm sh} \sim x^{-\beta_1 n}, \qquad (10)$$

where $\beta_1 \approx 0.18$ for common choices of $n = 3/2, 3$, corresponding to convective and radiative stellar envelopes, respectively. Its hydrodynamic profile follows the Sakurai-Weaver Anzats. Breakout occurs when the optical depth ahead of the shock is $\tau = c/v_{\rm bo}$. The breakout velocity $v_{\rm bo}$ and density $\rho_{\rm bo}$ are defined self-consistently at this time, where $\rho_{\rm bo}$ is the initial unshocked density profile at the shock location. At breakout the corresponding length of the shock is $l \sim c/\kappa\rho_{\rm bo}v_{\rm bo}$. The time scale for this breakout is $t_{\rm bo} = c/\kappa\rho v^2$, based on the shock crossing time scale. Following breakout, shock-heated material is expelled in the direction of the original shock.

The emitted bolometric luminosity for planar shock breakout was given semi-analytically by Sapir et al. (2011) as a function of $\rho_{\rm bo}$, $v_{\rm bo}$. The peak luminosity per unit area is approximately given by $\mathcal{L}_{\rm peak} \approx \rho_{\rm bo}v_{\rm bo}^3$ corresponding to the shock's energy.

Similarly to the previous discussion in the uniform RMS problem, opacity is dominated by free-electron scattering. The hydrodynamics (ρ, v, p) and bolometric breakout luminosity are insensitive to the photon production mechanism, though temperature T and radiation distribution $u_\nu(r,t)$ and correspondingly the breakout spectrum, can be greatly affected. In cases where the photon production is efficient within a shock crossing time, the radiation will match a Planck spectrum $u_\nu = B_\nu(T)$. The temperature everywhere in this case is very nearly given by

$$T_{\rm LTE,SW} = [3P_{\rm SW}/a_{BB}]^{1/4}, \qquad (11)$$

where $P_{\rm SW}(r,t)$ is the pressure in the Sakurai-Weaver Anzats (Sapir et al. 2011, different from $P_{\rm S}$ in equation 5), which describes well the pressure in the simulation.

For fully ionized Bremsstrahlung emission, Sapir et al. (2013) provide an analytic formula for the planar shock breakout peak emission temperature $\mathcal{T}_{\rm peak}$ and a semi-analytic description for the time-dependent emission

temperature $\mathcal{T}(t)$, given by

$$
\begin{aligned}
\log_{10}\left(\frac{\mathcal{T}_{\rm peak}}{10 \text{ eV}}\right) &= 1 + 1.69\,\beta_{-1}^{1/2} \\
&+ \left(0.26 - 0.08\,\beta_{-1}^{1/2}\right)\log_{10}\left(An_{\rm p,15}\right), \quad n = 3 \\
\log_{10}\left(\frac{\mathcal{T}_{\rm peak}}{10 \text{ eV}}\right) &= 0.95 + 1.78\,\beta_{-1}^{1/2} \\
&+ \left(0.26 - 0.08\,\beta_{-1}^{1/2}\right)\log_{10}\left(An_{\rm p,15}\right), \quad n = 3/2,
\end{aligned}
$$
$$(12)$$

where $\beta_{\rm bo} = 0.1\beta_{-1}$, A is the ion mass in atomic mass units, and $n_p = 10^{15}n_{p,15}$. The formulas were calibrated against a set of gray simulations (with 10% agreement) counting total photon production rate $\dot{n}_\gamma(r,t)$ and assuming Compton equilibrium. They found that peak temperature occurs roughly one shock-crossing time prior to peak luminosity time.

4.2. Initial and Boundary Conditions

Our numeric simulation describes an RMS shock traversing in a cold medium, with initial matter density $\rho_{\rm init} = \rho_{\rm bo}\left(\beta_{\rm bo}\tau\right)^{n/(n+1)}$, where $x = 0$ and $\tau = 0$ represents the stellar edge. We introduce the terms 'inner' and 'outer' edges to denote densest and least dense simulated edges of the problem (respectively), in analogy to the geometry of a stellar explosion. For faster convergence, initial shock hydrodynamics are started using the Sakurai-Weaver approximation Sapir et al. (2011). The inner piston at the high density edge is taken to be the Sakurai (1960) solution. The photons and the plasma are initially assumed to be in LTE (Planck distributed in agreement with a local plasma temperature T).

Similarly to the initial spatial grid in Morag et al. (2023) and M24, our spatial resolution is a smooth function of position, described consecutively from the piston to the outer edge as follows. We place modest resolution near the piston, highest resolution at the initial shock location, gradually decreasing resolution towards the edge (for constant cell number across the progressing RMS shock), flat resolution for $\tau \lesssim c/v$, and increasing resolution towards the outer edge ($\tau < 10^{-2} - 10^{-3}$). Simulations are started between 4-8 shock crossing distances away from the stellar edge, and are shown to be largely insensitive to the choice of distance. We employ a multigroup frequency grid of $\Delta\nu/\nu \sim 0.07 - 0.25$. Unless otherwise indicated, all sims are converged to better than 2-3% in ρ, v, p, as well 3% in peak T and $10's$ of percent in emitted spectral energy distribution (SED) L_ν at individual frequencies. We also check convergence with respect to initial pre-shock temperature, minimum optical depth in the outermost cell ($\tau \sim 10^{-2} - 10^{-3}$),

and location of the piston relative to the starting shock location.

To avoid numeric issues associated with the presence of strong lines at low temperatures, in some of the SBO simulations we reduce the multigroup opacity table for the range $h\nu > \chi \equiv 200$ eV to its value at $h\nu = \chi$, only if the former is higher. Namely we make the substitution, $\kappa_{\mathrm{abs},\nu}(h\nu > \chi) \rightarrow \min[\kappa_{\mathrm{abs},\nu}(h\nu = \chi), \kappa_{\mathrm{abs},\nu}(h\nu > \chi)]$. Reducing peaks in this way does not negate our conclusions as long as the photons remain in LTE, since we are only reducing κ (photon production) and never increasing it. This substitution is made for all simulations with $\rho_{\mathrm{bo}} = 10^{-11}$ g cm^{-3}, and for $n = 3/2$, $\rho_{\mathrm{bo}} = 10^{-9}$ g cm^{-3} $\beta_{\mathrm{bo}} \leq 0.02$, and $n = 3$, $\rho_{\mathrm{bo}} = 10^{-9}$ g cm^{-3} for all values of β_{bo}. In the same simulations we use a script of snapshots of the hydrodynamics for (ρ, v) from a gray diffusion simulation started with the exact same initial conditions and resolution (see description of the numerics in Morag et al. 2023). Convergence is achieved to the same extent in all cases.

4.3. *Planar SBO Temperature Results*

We present numeric results for the planar shock-breakout problem, in two separate sets of simulations, (1) with free-free only emission, and (2) with TOPS opacity. The hydrodynamics and bolometric luminosity are insensitive to the choice of opacity. The hydrodynamics (ρ, v, p) agree with the Sakurai-Weaver solution (Sapir et al. 2011), to better than 2% for all simulations[6] for the times $t/t_{\mathrm{bo}} = -3, -5$ with no fitting of any kind. At shock breakout at low velocities ($\beta \lesssim 0.1$) we find good agreement (3% or better) between the bolometric luminosity in the simulations and the semi-analytic shock breakout description, given in L_{SKW}. For higher velocities, the bolometric luminosity can deviate from L_{SKW} by up to 15%, in agreement with SH14. The deviation is expected, and is due to the use of the Eddington approximation at the outer edge of the material (see discussion SH14 in sec. 4.3).

An example of the effects of opacity on planar shock breakout are shown in figures 5 and 6 for the case $\beta_{\mathrm{bo}} = 0.1$, $\rho_{\mathrm{bo}} = 10^{-9}\,\mathrm{g\,cm}^{-3}$, exhibiting similar behavior to the uniform RMS problem. Figure 5 shows an example temperature profile. For Bremsstrahlung only (dashed lines), electron temperature and photon temperature deviate largely from T_{LTE} and are coupled in Compton equilibrium at the shock and immediately downstream of it. At shock breakout, T will reach ~ 500 eV, in $\lesssim 10\%$ agreement with equation 12. We observe

a radiative precursor, similarly to the uniform RMS case and in agreement with SH14. Meanwhile, when TOPS opacity is included (solid lines), the temperature at peak remains much closer to LTE (~ 150 eV), and thermalizes more quickly in the downstream. During shock breakout, temperature upstream of the peak (towards the outer edge), decreases relative to the peak temperature.

Figure 6 shows an example of the SED output spectrum near shock breakout, for the same simulations as in figure 5. When Bremsstrahlung is used, photons above the critical frequency $h\nu_{\mathrm{c}} \sim 1eV$ (see sec. 3.1) up-scatter with the hot electrons to temperature $\sim 3T$. The up-scattered photons dominate the spectrum, with typical temperature T_γ and a Comptonized Wien spectrum, in agreement with the semi-analytic description of Sapir et al. (2013) (hereafter SKWIII, teal dashed lines). At frequencies below $h\nu_{\mathrm{c}}$, the photons are in thermal equilibrium with the plasma, forming a Planck spectrum with the same temperature $B_\nu(T)$ (black dashed lines). No fitting or rescaling is performed during the comparison to SKWIII.

When TOPS opacity is included in figure 6 (solid lines), the emission is similar to a Planck profile (example in solid black line for t=0). 10's of percent deviations from Planck are observed in the shape of the SED, primarily at intermediate frequencies ($h\nu \sim 10$ eV). At these frequencies, there are no atomic transition lines, and the emission opacity is relatively low. As a result, photons that would eventually escape the ejecta are produced deeper inside at larger optical depths, and their outward flux is suppressed by scattering. Outside of these frequencies there is larger opacity (free-free processes at lower frequencies and atomic transition lines at higher frequencies), and the spectrum is relatively close to Planck. At frequencies above the Planck peak, where atomic lines are generally strong, the emission is slightly reduced by line damping. These SED shape results are very similar to those of M24, and we refer the reader to an in-depth discussion there.

Figures 7 and 8 provide a mapping of the peak emitted breakout temperature as function of $(\rho_{\mathrm{bo}}, \beta_{\mathrm{bo}})$, for $n = 3/2$ and $n = 3$, respectively. Simulation results in the case of free-free opacity (solid blue lines) are in good agreement with the analytic formula by Sapir et al. (2013, equation 12 - green lines), calculated assuming Compton equilibrium. At low velocities ($\beta \lesssim 0.02$) in the presence of free-free opacity only, the radiation at the shock remains near LTE. Photons that escape during breakout are produced at $\tau \sim c/v_{\mathrm{bo}}$ (the immediate downstream), where the pressure is $p \sim \rho_{\mathrm{bo}} v_{\mathrm{bo}}^2$. Therefore, the peak emission temperature at these low veloci-

---

[6] See also example agreement with T_{LTE}, figure 5 prior to shock breakout.

ties is approximately described to 10's of percent by eq. 9 that was introduced in the context the uniform radiation mediated shock, but with $\rho_{\rm bo}$ and $v_{\rm bo}$ replacing ρ_0 and v_0 (red dashed line).

The situation is different when bound-free and bound-bound processes are introduced (yellow lines). At slow velocities, photons produced at $\tau \sim \beta^{-1}$ reprocess on the way out towards the outer edge. Therefore, the emitted temperature represents the local temperature at $\tau \sim 1$, which itself is determined self-consistently by the outgoing flux. Therefore, the emission temperature at low velocities is well approximated as

$$T_{\rm LTE,\mathcal{L}} = (4\,\mathcal{L}_{\rm SKWI}\,/c\,a_{\rm BB})^{1/4}, \qquad (13)$$

where $\mathcal{L}_{\rm SKWI}(t)$ is the semi-analytic solution for the bolometric breakout luminosity, provided in Sapir et al. (2011). Then the peak luminosity (magenta line in figures 7 and 8) is

$$T_{\rm LTE,\mathcal{L}peak} = (4\,(a_{\rm L}\rho_{\rm bo}v_{\rm bo}^3)\,/c\,a_{\rm BB})^{1/4}, \qquad (14)$$

where $a_{\rm L} = (0.72, 0.77)$ for $n = 3/2, 3$ are the coefficients in Sapir et al. (2011) representing the peak luminosity[7]. Everywhere where equation 13 holds, and significant reprocessing of the photons occurs towards $\tau \sim 1$, the observed emission temperature is at least a factor of two lower than the predicted temperature in the case of free-free only[8]. The opacity change also affects the time of peak temperature. For the free-free only case, $\mathcal{T}_{\rm peak}$ occurs roughly a shock crossing time prior to the time of peak luminosity (Sapir et al. 2013), but with TOPS the $\mathcal{T}$ and $\mathcal{L}$ peaks coincide.

At higher velocities in the presence of TOPS, there is eventually a transition to a Comptonized (or partially Comptonized) output spectrum, tending towards the previous free-free temperature result (equation 12). This transition implies both a reduced relative photon production rate at the peak due to high ionization, as well as limited reprocessing of the photons as they traverse from $\tau \sim c/v$ to $\tau \sim 1$. At highest densities ($\rho_{\rm bo} = 10^{-7}$ g cm^{-3}), the transition to Compton behavior begins at lower velocities, $\beta_{\rm bo} \lesssim 0.03$. At lowest densities ($\rho_{\rm bo} = 10^{-11}$ g cm^{-3}), the transition is barely
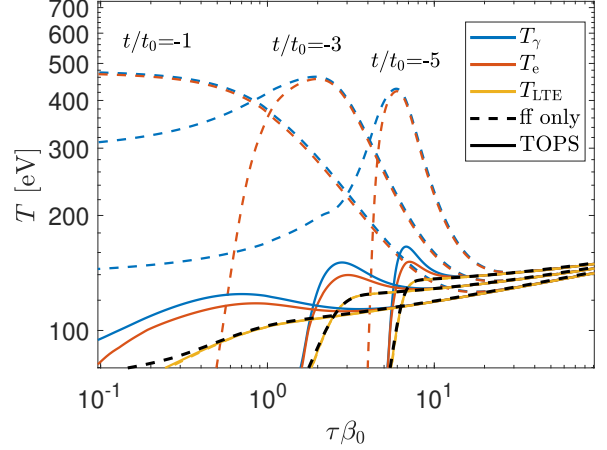

Figure 5. Snapshots of the temperature, 1 3 and 5 shock crossing times prior to shock breakout, for the choice $\rho_{\rm bo} = 10^{-9}$ g cm^{-3} and $\beta_{\rm bo} = 0.1$. Peak temperature at the shock is much lower with TOPS opacity (solid lines - color) relative to ff-only (dashed lines -color). The equivalent LTE tempeature (yellow lines) are compared to the Sakurai-Weaver Anzats (black dashed lines) showing excellent agreement. The legend only refers to the colored lines. The dashed black line is equation 11 based on the Sakurai-Weaver Anzats, added to show good agreement with the numerics.

observed at all, leading to a possible orders of magnitude difference in emission temperature when TOPS opacity is added.

Mapping the parameter space in the cases of bound-free and bound-bound opacity was not everywhere possible, partially due to numerical issues associated with the use of the TOPS table. In some cases, our simulations were converged to 10's of percents. In figures 7 and 8 we show some of these partially converged results in order to qualitatively demonstrate the transition towards 'Comptonized' behavior (yellow dashed lines without dots). We also note that our temperature results at the transition are limited in their validity to a certain extent since our opacity assumes the plasma to be in thermal equilibrium with the radiation, which is not the case there. Presumably at even higher temperatures, where the plasma is nearly fully ionized, this concern is again less important.

5. DOPPLER BROADENING AND FINITE

Our code does not include expansion opacity and includes a finite frequency grid that is much coarser than the atomic line widths and the frequency separation between lines. As such, there is concern that strong lines can lead the simulation code to overestimate photon production (see in depth discussion in M24). Similarly to M24, we show here that Doppler broadening of the lines

---

[7] As a sanity check, we also extract the equivalent temperature from $T_{\rm Lsim,LTE} = (4\mathcal{L}/c\,a_{\rm BB})^{1/4}$, where $\mathcal{L}$ is the bolometric luminosity extracted from the simulation. The result is the same as equation 13

[8] For part of the parameter space, Compton equillibrium and deviation from LTE can be achieved at t=c/v during shock breakout, but emission can still be at LTE and agree with equation 13 due to reprocessing up to tau=1 (e.g. high velocities at low densities - $\rho_{\rm bo} = 1e-11$ g cm^{-3}, $\beta_{\rm bo} = 0.1$).
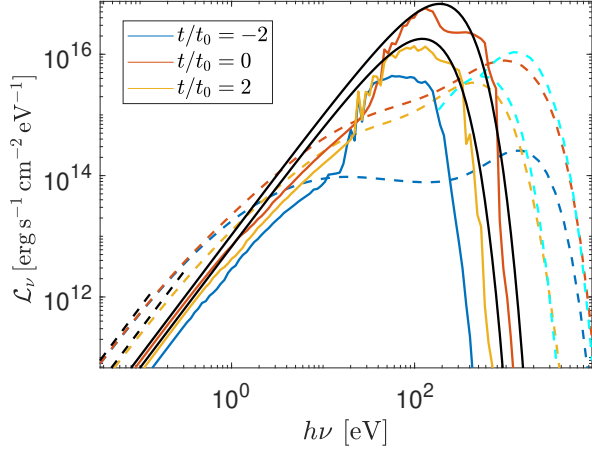
Figure 6. Output spectrum from the same simulations as figure 5, shown near shock-breakout time. The spectrum at breakout in the case of free-free only opacity (dashed lines) is dominated by a Compton peak, in agreement with the semi-analytic description from SKWIII (teal dashed lines). The output spectrum in the case of TOPS opacity (solid colored lines) is well described a Planck spectrum with $T_{\mathrm{LTE},\mathcal{L}}$ (solid black lines - equation 13).
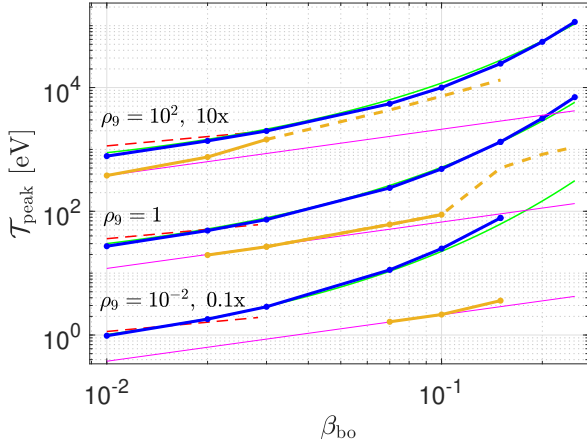

Figure 7. Mapping of peak emission temperature as a function of $(\rho_{\mathrm{bo}}, \beta_{\mathrm{bo}})$ for density profile with $n = 3/2$ (see text). Temperatures are visibly reduced in the presence of bound-free and bound-bound opacity due to reprocessing. We rescale the temperatures for lowest and highest densities for improved visibility. ρ_9 is defined by $\rho_{\mathrm{bo}} = 10^{-9}\rho_9$ g cm^{-3}.

and the presence of a line forest in this problem, can smear the atomic line forest to an extent that greatly reduces the unevenness in u_ν across a frequency grid point, qualitative supporting the validity of our results. See an example in figure 9, showing smearing of lines in $\rho\kappa_\nu$ across $\tau \sim c/v$ due to line expansion, where τ is the electron scattering opacity.
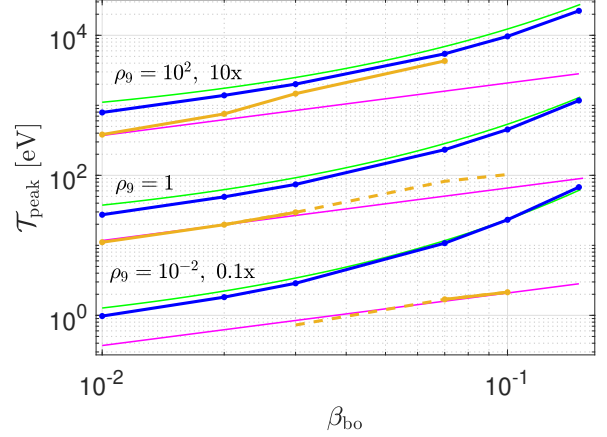

Figure 8. Same as figure 7, but with $n = 3$.

A second effect that is expected to smear u_ν during shock breakout is inelastic Compton scattering. Prominent lines in shock breakout temperatures can be relatively weak (e.g. $\kappa_\nu \sim O(1)$ cm^2 g^{-1})[9]. Therefore, at breakout temperatures, the chance that a photon will escape resonance via Compton scattering with a cross section $\kappa_{\mathrm{es}} \sim 0.34$ cm^2 g^{-1} becomes non-negligible.

A single Compton scattering will shift the photon by $\Delta\nu/\nu \sim T/m_{\mathrm{e}}c^2$. For example, at $T = 50$ eV, $\Delta\nu/\nu \sim 10^{-4}$, a Doppler shift which is larger than the natural width of a line and comparable with the thermal line width $\Delta\nu/\nu \sim \sqrt{3T/Am_{\mathrm{p}}} = 5 \times 10^{-5}$, where we chose $A = 55 - 65$. If a photon is scattered to a frequency and direction that will allow it to escape Doppler expansion opacity, it may escape resonance. Once outside of resonance, it should Compton scatter multiple times and efficiently diffuse in frequency.

In a previous work, we performed a relaxation rate analysis, concluding that LTE should be conserved up to recombination. Here, due to the relative higher density, we do not repeat this analysis and assume that the plasma degrees of freedom remain in LTE so long as the radiation does not deviate largely from Planck emission.

6. OBSERVATIONAL IMPACT

Here we estimate the effect that the introduction of atomic lines in the opacity will have on SN observations, including in X-ray. We estimate ρ_{bo} and β_{bo} for various types of progenitor stars using equations summarized in

---

[9] The situation is very different during shock cooling (e.g. $T \sim 1$ eV), where inelastic Compton scattering is weak, and line strengths can reach $\kappa_\nu \sim O(10^6)$ cm^2 g^{-1}.
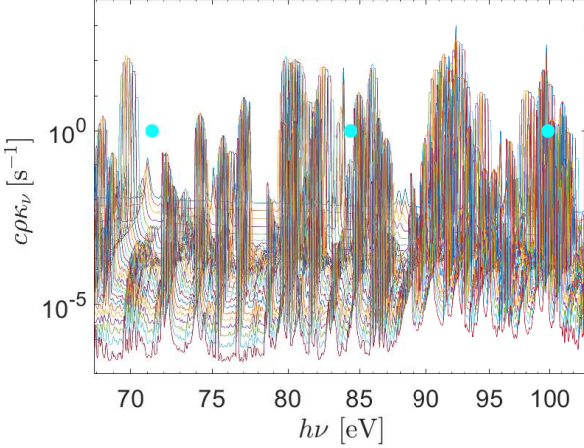
Figure 9. Example high-resolution TOPS opacity extracted using (ρ, T) from our simulation. Here $(n = 3/2,\ \rho_{\mathrm{bo}} = 10^{-9}\,\mathrm{g\,cm}^{-3},\ \beta_{\mathrm{bo}} = 0.1)$. Plasma temperatures are in the range 60-100 eV, the time is t=0, corresponding with breakout in the equivalent Sakurai problem. Each grid location is Doppler shifted and smeared according to v and Δv from the same simulation. Only grid cells for $\tau < c/v$ are shown. The three large teal dots provide an example of the frequency edges of the binned multigroup photon groups.

Waxman & Katz (2016). For red super giants:

$$\rho_{\mathrm{bo}} = 1.16 \times 10^{-9} M_0^{0.32} \mathrm{v}_{*,8.5}^{-0.68} R_{13}^{-1.64} \kappa_{0.34}^{-0.68} f_\rho^{0.45}\ \mathrm{g\,cm}^{-3},$$
$$\mathrm{v}_{\mathrm{bo}}/\mathrm{v}_* = 3.31 M_0^{0.13} \mathrm{v}_{*,8.5}^{0.13} R_{13}^{-0.26} \kappa_{0.34}^{0.13} f_\rho^{-0.09}. \tag{15}$$

For blue super giants:

$$\rho_{\mathrm{bo}} = 3.1 \times 10^{-10} M_0^{0.13} \mathrm{v}_{*,8.5}^{-0.87} R_{13}^{-1.26} \kappa_{0.34}^{-0.87} f_\rho^{0.29}\ \mathrm{g\,cm}^{-3},$$
$$\mathrm{v}_{\mathrm{bo}}/\mathrm{v}_* = 4.1 M_0^{0.16} \mathrm{v}_{*,8.5}^{0.16} R_{13}^{-0.32} \kappa_{0.34}^{0.16} f_\rho^{-0.05}, \tag{16}$$

Based on these, we adopt the fiducial values given in SKWIII,

$$\beta_{\mathrm{bo}} = 0.05 M_{10}^{0.13} v_{*,8.5}^{1.13} R_{13}^{-0.26} \kappa_{0.4}^{0.13} f_\rho^{-0.09} \quad (\mathrm{RSG})$$
$$= 0.14 M_{10}^{0.16} v_{*,8.5}^{1.16} R_{12}^{-0.32} \kappa_{0.4}^{0.16} f_\rho^{-0.05} \quad (\mathrm{BSG}) \tag{17}$$
$$= 0.23 M_5^{0.16} v_{*,8.5}^{1.16} R_{11}^{-0.32} \kappa_{0.2}^{0.16} f_\rho^{-0.05} \quad (\mathrm{WR})$$

and

$$\rho_{\mathrm{bo}} = 2 \times 10^{-9} M_{10}^{0.32} v_{*,8.5}^{-0.68} R_{13}^{-1.64} \kappa_{0.4}^{-0.68} f_\rho^{0.45}\ \mathrm{g\,cm}^{-3}\ (\mathrm{RSG})$$
$$= 7 \times 10^{-9} M_{10}^{0.13} v_{*,8.5}^{-0.87} R_{12}^{-1.64} \kappa_{0.4}^{-0.87} f_\rho^{0.45}\ \mathrm{g\,cm}^{-3}\ (\mathrm{BSG})$$
$$= 2 \times 10^{-7} M_5^{0.13} v_{*,8.5}^{-0.87} R_{11}^{-1.26} \kappa_{0.2}^{-0.87} f_\rho^{0.29}\ \mathrm{g\,cm}^{-3}\ (\mathrm{WR}), \tag{18}$$

where the progenitor radius is $R = 10^x R_x$, and total mass is $M = x M_\odot M_x$, and $M_\odot$ is the solar mass.

Using equation 15, we estimate the parameter range for RSG explosions, from a sample of 33 type II SNe

in Irani et al. (2023) - table 4. From light curve fits, they deduce progenitors in the range $R_{13} = 3 - 18$, and $v_{*,8.5} \approx 0.3 - 2$[10]. This range of radii (in particular the lower values) is confirmed by the observed distribution of RSG's in the Magellenic clouds from Davies et al. (2013) - see text in Irani et al. (2023). As $f_\rho M$ is not discernible from early shock-curve fitting, we adopt $M = 10 M_\odot$, where $M_\odot$ is the solar mass, and $f_\rho \sim 1$, with minor effect on parameters. We estimate therefore that explosions in RSG's primarily lie in the range $\rho_{\mathrm{bo}} \sim 10^{-11} - 3 \times 10^{-10}\ \mathrm{g\,cm}^{-3}$, $\beta_{\mathrm{bo}} \sim 0.01 - 0.05$, and therefore conclude that deviations from LTE for envelope breakout in RSG's are unlikely. This conclusion also holds for a more conservative value of $R_{13} = 1$, i.e., the fiducial value $\beta_{\mathrm{bo}} = 0.05$, $\rho_{\mathrm{bo}} = 2 \times 10^{-9}\ \mathrm{g\,cm}^{-3}$ given in equations 17 - 18.

As a demonstration of the effect of temperature on type II SN observations, we show in figure 10 light curve results in the Swift XRT band derived from SED's in our simulations. We choose an example $R = 3 \times 10^{13}$ cm, $\rho_{\mathrm{bo}} = 10^{-9}\ \mathrm{g\,cm}^{-3}$, and $\beta_{\mathrm{bo}} = 0.03$. The choice of radius enters into the luminosity description $L_\nu = 4\pi R^2 \mathcal{L}_\nu$, where $\mathcal{L}_\nu$ is the planar SED from simulation. Radius also affects the emission due to light-travel time effects, which we include in the figure. These smear the observed emission in time by $t \sim R/c$, given by (Katz et al. 2012)

$$L_{\nu,\,\mathrm{obs}}(t) = \int_0^1 h(\mu) L_\nu(t - R(1-\mu)/c)\mu d\mu, \tag{19}$$

where $h(\mu) = 0.85 + 1.7\mu$.

In the presence of atomic lines in the above example, the peak equivalent photon temperature (equation 4) is $\mathcal{T}_{\mathrm{peak}} = 27$ eV, a factor of 2 lower than the case with free-free only opacity, $\mathcal{T}_{\mathrm{peak}} = 73$ eV. Consequently, the flux in the XRT band ([0.3,10] keV), which lies in the Wien tail for both of these SED's, is lowered in the presence of TOPS by 3 orders of magnitude. In lower velocity and density simulations we find the X-ray flux, which is already exceedingly small $\sim 10^{38}\ \mathrm{erg\,s}^{-1}$, can be reduced by even more orders of magnitude ($\sim 10^{30}\ \mathrm{erg\,s}^{-1}$). Therefore, we conclude that the addition of atomic lines in the opacity reduces the volume of 'envelope breakout' objects with observable X-Ray emission by at least $\sim (10^{-3})^{3/2} = 3 \times 10^{-5}$ or even more (ignoring extinction), with sensitivity of this result to the low radius (higher β_{bo}) distribution of RSG progenitors.

In blue super giants, the fiducial parameters for explosions based on equations 17 - 18, are $\rho_{\mathrm{bo}} = 7 \times$

---

[10] We employ the approximation $v_{s*} \approx 1.05 f_\rho^{-0.19} v_* \approx v_*$.
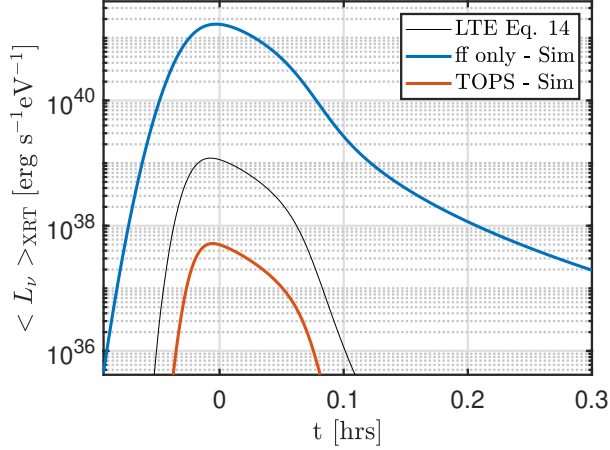
Figure 10. Demonstration of predicted X-ray shock breakout luminosities in the range [0.3,10] keV, representative of the Swift satellite XRT band and the Einstein Probe satelite. There is a ~ 3 orders of magnitude difference in emitted energy between ff only and TOPS simulations. The approximate equation 13 agrees with the TOPS simulation up to an order of magnitude, as it does not include line dampening, which is important for part of the parameter space. This plot includes light travel time effects (equation 19).

10^{-9} g cm^{-3} and $\beta_{\rm bo} = 0.14$. SN 1987a, whose progenitor star exhibits $R \approx 3 \times 10^{12}$ cm, $M \sim 10 M_\odot$ (Arnett et al. 1989) exhibits similar breakout parameters. Based on the results in figure 8, these values fall in the transition region, where the radiation distribution slightly deviates from local thermal equilibrium, but likely does not reach temperatures high enough to exhibit fully ionized Bermsstrahlung opacities (equation 12). As blue super giant stars span a range, we expect some significant fraction of explosions from larger radius BSG's to remain in LTE following equation 13, and the rest (at the fiducial value and above) to exhibit somewhat higher temperatures. Due to uncertainty regarding the TOPS opacities (and line transitions in general), the exact turn-off point in parameter space as well as the exact behavior in this intermediate region of the parameter space is difficult to predict.

Finally, Wolf-Reyet stars, which exhibit substantially smaller radii, and therefore significantly higher breakout densities and velocities (10^{-7} g cm^{-3}, $\beta_{\rm bo} \gtrsim 0.2$), will likely be fully ionized. Therefore, their observations should be unaffected by the the results of this paper.

7. DISCUSSION AND SUMMARY

In this paper we numerically studied the uniform radiation mediated shock and the planar shock breakout problems, including for the first time, the effects of bound-free and bound-bound radiative processes. We found that for both systems, due to increased photon production, these processes can at times significantly delay deviations from local thermal equilibrium that were previously predicted for high velocities ($\beta \gtrsim 0.07$-0.1 - Weaver 1976; Katz et al. 2010; Sapir et al. 2013).

In sec. 3.1, we numerically solved the uniform RMS problem with both free-free only and TOPS (free-free, bound-free, bound-bound) opacity. In figure 3, we mapped the shock velocity and initial density parameter space ($\rho_0 = 10^{-11} - 10^{-7}$ g cm^{-3} and $\beta_0 = c/v_0 = 0.01 - 0.25$). In the free-free case, we observed temperature deviations from LTE towards Compton equillibrium, confirming previous analytic and semi-analytic estimates (equation 8). We found that for lowest densities, $\rho_0 = 10^{-11}$ g cm^{-3}, peak photon temperature when using TOPS opacities can remain in LTE (equation 5) at high velocities. Meanwhile, at highest densities $\rho_0 = 10^{-7}$ g cm^{-3}, peak temperature is only mildly affected by the addition of bound-free and bound-bound opacity.

We perform a similar analysis of the planar shock breakout problem in § 4, including a mapping of peak temperature in figures 7 and 8 for initial density profiles $\rho \sim x^{3/2}$ and x^3, respectively. For free-free only simulations, peak temperature at shock-breakout is defined by the local temperature at an optical depth $\tau \sim c/v$. The observed peak Wien emission is well described to 10's of percent by equation 12 from the literature, which assumes Compton equillibrium, in agreement with the literature.

When TOPS opacity is employed in planar shock breakout, the production of additional photons can delay deviations from LTE. At emission temperatures $\mathcal{T} \lesssim 100$ eV, photons get reprocessed as they escape. As we showed in figure 6, the emission is then will described by a blackbody $\mathcal{L}_\nu = \pi B_\nu$ with temperature given by equation 13 (our main analytic result - rewritten here)

$$\mathcal{T}_{\rm LTE,\mathcal{L}}(t) = (4\,\mathcal{L}_{\rm SKWI}\,/c\,a_{\rm BB})^{1/4}. \qquad (20)$$

$\mathcal{L}_{\rm SKWI}$ is the Sapir et al. (2011) bolometric breakout luminosity, provided as a table. Then the emission temperature at peak time is given by

$$\mathcal{T}_{\rm LTE,\mathcal{L}peak} = (4\,(a_{\rm L}\rho_{\rm bo}v_{\rm bo}^3)\,/c\,a_{\rm BB})^{1/4}. \qquad (21)$$

When LTE is maintained, these temperatures are at least a factor of 2 lower than the equivalent temperatures in the case of free-free only opacity. At higher velocities and temperatures ($T \gtrsim 100$ eV), the system leaves LTE and transitions towards Compton equillilbrium even in the presence of atomic lines. In this instance the emission is determined again at $\tau \sim c/v$, and peak emission temperature behaves according to equation 12.

Our results affect the predictions for envelope shock breakout observations, especially with regards to x-ray (less so in the UV), shown in § 6. In figure 10 we show the effect on X-rays. For explosions in red super giants, strong deviations from LTE in breakout emission are unlikely. The deviation between our results and the previous literature prediction (SKWIII) is roughly a factor of 2^{11}. Explosions from BSG's lie at the transition in behavior, such that for envelope breakout a fraction of them will remain near LTE, and a fraction may transition towards a Comptonized emission spectrum. Our results do not affect breakout from Wolf-Reyet stars, nor do they have an effect on predictions for GRB's associated with SBO. We also do not consider breakout in wind or circumstellar material which can lead to much different emission due to the presence of a collisionless shock.

Velocity is an important predictor for the extent of deviations from LTE, especially in the case of free-free opacity. However, when bound-free and bound-bound processes are included, our mapping indicates that a primary factor that dictates the extent to whether T_{peak} will deviate from LTE is temperature (primarily the corresponding T_{LTE}), due its effect on opacity.

Our results were performed with the case of a solar mix of elements. For lower metallicity compositions, the photon production due to line emission may be reduced. We note however, that the shift away from LTE occurs primarily when the lines disappear altogether, such that we do not expect a slightly lower metallicity to have a pronounced effect on the result for much of the parameter space (similarly to M24). Other systems where Hydrogen has been depleted (say in C/O dominated systems) the relative metallicity of heavy elements would only increase, along with the tendency to remain in LTE. A further study of the effect of metallicity on deviations from LTE is beyond our scope.

In Morag (2023) we produced a frequency-dependent opacity table for arbitrary mixtures, based on the Kurucz atomic line list (see description in M24). Kurucz contains atomic lines that are calibrated against experiment for temperatures near Hydrogen recombination ($T \sim 1\,\mathrm{eV}$). The most ionized states for heavy elements are not included. At breakout temperatures, where only the most ionized states (not fully ionized) from heavy elements contribute to the absorption opacity, the difference in opacity can be pronounced. In figure 4, we provide an example of the multigroup opacity extracted from the hi-resolution opacity tables, TOPS and Morag (2023). At 40 eV, the averaged Morag (2023) opacity is many orders of magnitude lower the corresponding TOPS opacity. This difference would lead to a much lower photon production rate.

REFERENCES

Arnett, W. D., Bahcall, J. N., Kirshner, R. P., & Woosley, S. E. 1989, Annual Review of Astronomy and Astrophysics, 27, 629, publisher: Annual Reviews. https://www-annualreviews-org/content/journals/10.1146/annurev.aa.27.090189.002213

Blandford, R. D., & Payne, D. G. 1981, Monthly Notices of the Royal Astronomical Society, doi:10.1093/mnras/194.4.1033. http://paperity.org/p/39533190/compton-scattering-in-a-converging-fluid-flow-i-the-transfer-equation

Blinnikov, S., Lundqvist, P., Bartunov, O., Nomoto, K., & Iwamoto, K. 2000, The Astrophysical Journal, 532, 1132. https://doi.org/10.1086%2F308588

Bruch, R. J., Gal-Yam, A., Schulze, S., et al. 2021, The Astrophysical Journal, 912, 46, publisher: American Astronomical Society. https://doi.org/10.3847/1538-4357/abef05

Budnik, R., Katz, B., Sagiv, A., & Waxman, E. 2010, The Astrophysical Journal, 725, 63, arXiv: 1005.0141. http://arxiv.org/abs/1005.0141

Campana, S., Mangano, V., Blustin, A. J., et al. 2006, Nature, 442, 1008. http://www.nature.com/nature/journal/v442/n7106/abs/nature04892.html

Colgan, J., Kilcrease, D. P., Magee, N. H., et al. 2015, High Energy Density Physics, 14, 33. http://www.sciencedirect.com/science/article/pii/S1574181815000130

—. 2018, Atoms, 6, 32. https://www.mdpi.com/2218-2004/6/2/32

—. 2016, The Astrophysical Journal, 817, 116. https://doi.org/10.3847%2F0004-637x%2F817%2F2%2F116

Davies, B., Kudritzki, R.-P., Plez, B., et al. 2013, The Astrophysical Journal, 767, 3, publisher: The American Astronomical Society. https://dx.doi.org/10.1088/0004-637X/767/1/3

Dwarkadas, V. V. 2014, Monthly Notices of the Royal Astronomical Society, 440, 1917. https://doi.org/10.1093/mnras/stu347

Förster, F., Moriya, T. J., Maureira, J. C., et al. 2018, Nature Astronomy, 2, 808, number: 10 Publisher: Nature Publishing Group. https://www.nature.com/articles/s41550-018-0563-4

---

[11] (SKWIII) also do not predict strong deviations from LTE due to the low densities and velocities for RSG shock breakouts

Gandel'Man, G. M., & Frank-Kamenetskii, D. A. 1956, Soviet Physics Doklady, 1, 223, aDS Bibcode: 1956SPhD....1..223G. https://ui.adsabs.harvard.edu/abs/1956SPhD....1..223G

Gezari, S., Rest, A., Huber, M. E., et al. 2010, The Astrophysical Journal, 720, L77, publisher: American Astronomical Society. https://doi.org/10.1088/2041-8205/720/1/l77

Gezari, S., Jones, D. O., Sanders, N. E., et al. 2015, The Astrophysical Journal, 804, 28. http://stacks.iop.org/0004-637X/804/i=1/a=28

Huang, F., Wang, X.-F., Hosseinzadeh, G., et al. 2018, Monthly Notices of the Royal Astronomical Society, 475, 3959. https://doi.org/10.1093/mnras/sty066

Irani, I., Morag, J., Gal-Yam, A., et al. 2023, The Early Ultraviolet Light-Curves of Type II Supernovae and the Radii of Their Progenitor Stars, arXiv, arXiv:2310.16885 [astro-ph]. http://arxiv.org/abs/2310.16885

Ito, H., Levinson, A., & Nagataki, S. 2020a, Monthly Notices of the Royal Astronomical Society, 492, 1902. https://doi.org/10.1093/mnras/stz3591

Ito, H., Levinson, A., & Nakar, E. 2020b, Monthly Notices of the Royal Astronomical Society, 499, 4961. http://adsabs.harvard.edu/abs/2020MNRAS.499.4961I

Ivezić, Z., Kahn, S. M., Tyson, J. A., et al. 2019, The Astrophysical Journal, 873, 111, publisher: IOP Publishing. https://iopscience.iop.org/article/10.3847/1538-4357/ab042c/meta

Katz, B., Budnik, R., & Waxman, E. 2010, The Astrophysical Journal, 716, 781, arXiv: 0902.4708. http://arxiv.org/abs/0902.4708

Katz, B., Sapir, N., & Waxman, E. 2011, Proceedings of the International Astronomical Union, 7, 274. https://www-cambridge-org/core/journals/proceedings-of-the-international-astronomical-union/article/x-rays-rays-and-neutrinos-from-c

—. 2012, The Astrophysical Journal, 747, 147, arXiv: 1103.5276. http://arxiv.org/abs/1103.5276

Kozyreva, A., Nakar, E., Waldman, R., Blinnikov, S., & Baklanov, P. 2020, Monthly Notices of the Royal Astronomical Society, 494, 3927. https://doi.org/10.1093/mnras/staa924

Kurucz, R. L. 1995, in ASP Conference Series, Vol. 81, 583. http://adsabs.harvard.edu/abs/1995ASPC...81..583K

Levinson, A., & Nakar, E. 2020, Physics Reports, 866, 1, aDS Bibcode: 2020PhR...866....1L. https://ui.adsabs.harvard.edu/abs/2020PhR...866....1L

Margutti, R., Chakraborty, S., & Brown, P. 2013, ATel #5243: Swift XRT and UVOT detection of SN2013ej, , . https://www.astronomerstelegram.org/?read=5243

Morag, J. 2023, Frequency Dependent Opacity Table, Github. https://github.com/jon-morag/Freq_Dept_Opac_Table/

Morag, J., Irani, I., Sapir, N., & Waxman, E. 2024, Monthly Notices of the Royal Astronomical Society, 528, 7137. https://academic.oup.com/mnras/article/528/4/7137/7601374

Morag, J., Sapir, N., & Waxman, E. 2023, Monthly Notices of the Royal Astronomical Society, 522, 2764. https://doi.org/10.1093/mnras/stad899

Murase, K., Thompson, T. A., & Ofek, E. O. 2014, Monthly Notices of the Royal Astronomical Society, 440, 2528. https://doi.org/10.1093/mnras/stu384

Nakar, E., & Sari, R. 2012, The Astrophysical Journal, 747, 88. http://stacks.iop.org/0004-637X/747/i=2/a=88

Ofek, E. O., Arcavi, I., Tal, D., et al. 2014, The Astrophysical Journal, 788, 154. http://stacks.iop.org/0004-637X/788/i=2/a=154

Sakurai, A. 1960, COMMUNICATIONS ON PURE AND APPLIED MATHEMATIC, XIII, 353

Sapir, N., & Halbertal, D. 2014, The Astrophysical Journal, 796, 145. http://stacks.iop.org/0004-637X/796/i=2/a=145

Sapir, N., Katz, B., & Waxman, E. 2011, The Astrophysical Journal, 742, 36, arXiv: 1103.5075. http://arxiv.org/abs/1103.5075

—. 2013, The Astrophysical Journal, 774, 79, arXiv: 1304.6428. http://arxiv.org/abs/1304.6428

Shvartzvald, Y., Waxman, E., Gal-Yam, A., et al. 2023, ULTRASAT: A wide-field time-domain UV space telescope, arXiv, arXiv:2304.14482 [astro-ph], doi:10.48550/arXiv.2304.14482. http://arxiv.org/abs/2304.14482

Smith, N. 2014, Annual Review of Astronomy and Astrophysics, 52, 487. http://www.annualreviews.org/doi/10.1146/annurev-astro-081913-040

Soderberg, A. M., Berger, E., Page, K. L., et al. 2008, Nature, 453, 469. http://www.nature.com/nature/journal/v453/n7194/full/nature06997

Starling, R. L. C., Wiersema, K., & Levan, A. 2011, Discovery of a gamma-ray burst with an associated supernova, , , publication Title: arXiv e-prints ADS Bibcode: 2011arXiv1104.3087S, doi:10.48550/arXiv.1104.3087. https://ui.adsabs.harvard.edu/abs/2011arXiv1104.3087S

Tominaga, N., Morokuma, T., Blinnikov, S. I., et al. 2011, The Astrophysical Journal Supplement Series, 193, 20. http://stacks.iop.org/0067-0049/193/i=1/a=20

Wasserman, T., Sapir, N., Szabo, P., & Waxman, E. 2025,
    The Optical to X-ray Luminosity and Spectrum of
    Supernova Wind Breakouts, arXiv, aDS Bibcode:
    2025arXiv250400098W, doi:10.48550/arXiv.2504.00098.
    https://ui.adsabs.harvard.edu/abs/2025arXiv250400098W

Waxman, E., & Katz, B. 2016, arXiv:1607.01293 [astro-ph],
    arXiv: 1607.01293.   http://arxiv.org/abs/1607.01293

Waxman, E., & Loeb, A. 2001, Physical Review Letters, 87,
    071101.
    https://link.aps.org/doi/10.1103/PhysRevLett.87.071101

Weaver, T. A. 1976, The Astrophysical Journal Supplement
    Series, 32, 233.
    http://adsabs.harvard.edu/abs/1976ApJS...32..233W

Yuan, W., Zhang, C., Chen, Y., & Ling, Z. 2022, The
    Einstein Probe Mission, pages: 86 Publication Title:
    Handbook of X-ray and Gamma-ray Astrophysics ADS
    Bibcode: 2022hxga.book...86Y,
    doi:10.1007/978-981-16-4544-0-151-1.
    https://ui.adsabs.harvard.edu/abs/2022hxga.book...86Y

Zel'dovich, Y. B., & Raizer, Y. P. 2002, Physics of Shock
    Waves and High-Temperature Hydrodynamic
    Phenomena, annotated edition edn. (Mineola, N.Y:
    Dover Publications)

Zimmerman, E. A., Irani, I., Chen, P., et al. 2023,
    Resolving the explosion of supernova 2023ixf in Messier
    101 within its complex circumstellar environment, arXiv,
    arXiv:2310.10727 [astro-ph],
    doi:10.48550/arXiv.2310.10727.
    http://arxiv.org/abs/2310.10727